

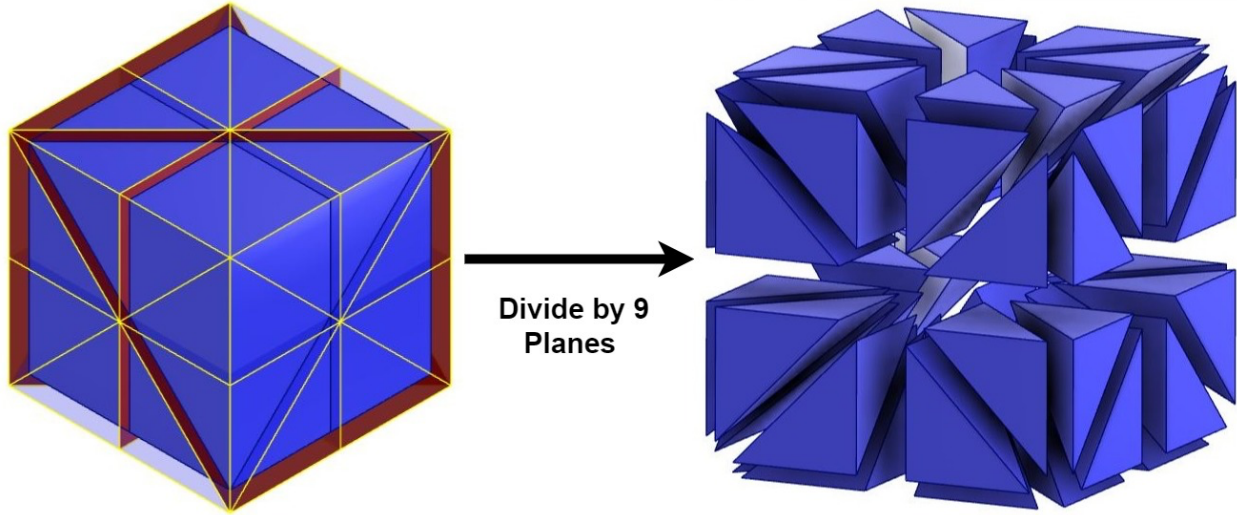
## Supplementary material

### DATA-GENERATION

In this section, our aim is to create a family of unit-cells that can be generated through a parametric method, thereby allowing for a wide range of material properties while remaining amenable to manufacturing processes. Although a multitude of unit-cells have been produced after the dominance of additive manufacturing, the majority of them lack the capacity for parametrization, and even those that do possess such capacity have limited material properties. To tackle these challenges, we propose a method that produces a broad and diverse set of parameterized data, not limited to Cubic and orthotropic structures. To achieve this, we employ the approach outlined in [1], which entails generating parametric cubic structures and subsequently modifying them by applying rotations to both the created truss structures and their points. This procedure results in a broad range of material properties, which we elaborate on later in this section.

#### Cubic Structure Generation Method

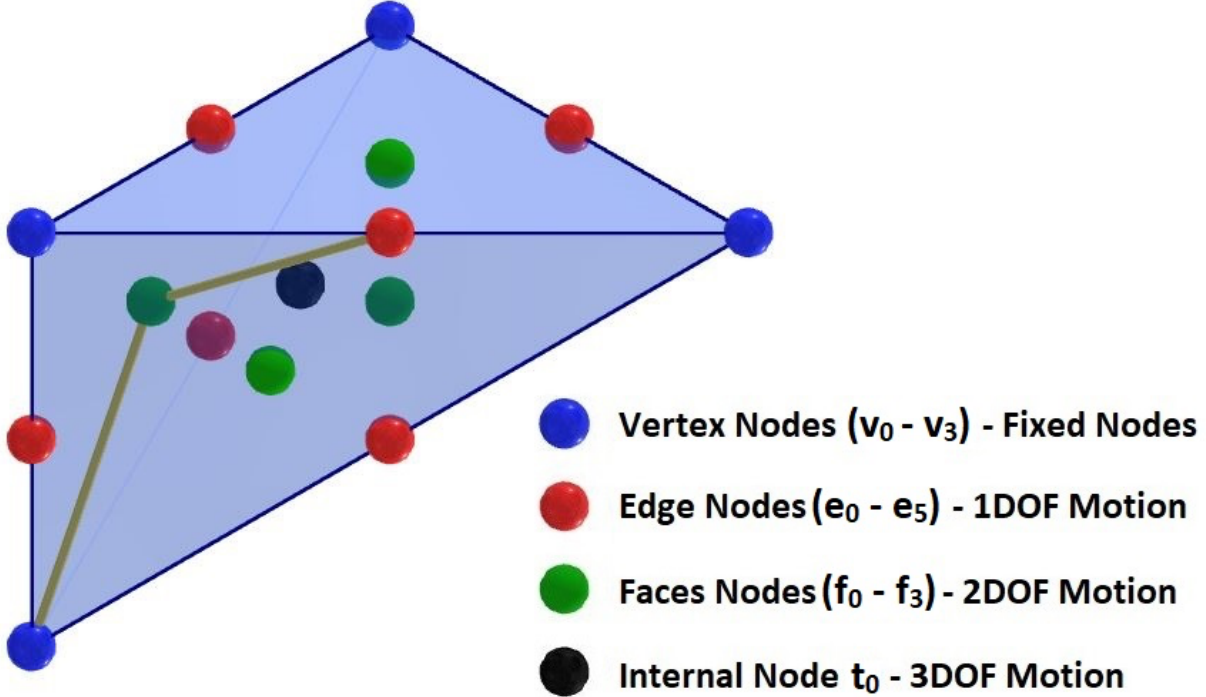
The establishment of a unit-cell's topological layout involves linking points within a cube with a set of edges in order to achieve the desired Cubic behavior. Based on the symmetries of the cube, nine planes of symmetry can be defined for any cubic material: three symmetry planes perpendicular to the primary cube axes and six planes perpendicular to the bisector of each pair of the primary three axes. By dividing a cube using these nine planes, it can be decomposed into 48 identical tetrahedrons, as illustrated in Supplementary Fig 1.



Supplementary Fig 1: The tetrahedral cube breakdown used to generate cellular structures.

Upon examination of a single tetrahedron, it is possible to identify fifteen distinct nodes, as demonstrated in Supplementary Fig 2. These nodes include vertex nodes ( $v_0, v_1, v_2, v_3$ ), which remain fixed in their respective locations within the tetrahedron, edge nodes ( $e_0, e_1, e_2, e_3, e_4, e_5$ ), each of which is capable of moving along a specific edge, face nodes ( $f_0, f_1, f_2, f_3$ ), which are capable of two-dimensional motion on a specific plane, and a single internal node ( $t_0$ ), which can

occupy any position within the tetrahedron. By varying the connections between these nodes and applying reflection along the nine symmetric planes previously mentioned, a vast number of unit-cell configurations can be generated. Moreover, it is noteworthy that these tetrahedrons possess symmetry, thereby causing the resulting cellular material to exhibit cubic symmetric behavior.

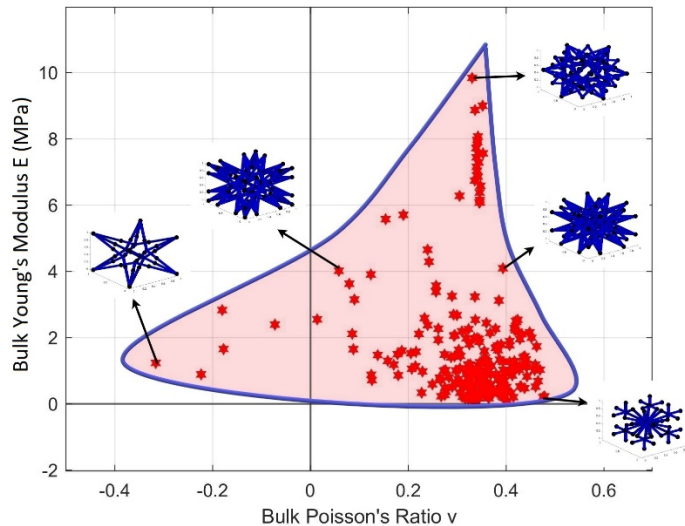


Supplementary Fig 2: The node of a single tetrahedron, and the motion space of each of the nodes.

The theoretical number of possible truss unit-cell configurations is extensive, with a potential upper limit of 1032. Nonetheless, a considerable proportion of these configurations may prove unviable for practical manufacturing purposes due to excessive complexity. Consequently, during the data generation phase, specific constraints were enforced to restrict the scope of the investigated structures. These constraints encompassed the following aspects:

- To ensure practical manufacturability, a constraint is imposed during data generation based on the use of stereolithography printers. This constraint requires that every node used in constructing the unit-cell possess a valence greater than one after reflection along symmetry axes, guaranteeing both connectivity and printability.
- Two additional constraints are enforced to limit the complexity of the unit-cell configurations. The first constraint limits the valence to a maximum of seven, while the second constraint imposes a maximum of three edges per tetrahedron.
- A further constraint was implemented to eliminate overlapping edges within the collection of edges. Specifically, when selecting an edge, such as  $(v_2, v_3)$ , any smaller edges contained within it, such as  $(v_2, e_2)$  and  $(e_2, v_3)$ , have to be excluded from the collection if they overlapped with the first edge, regardless of the offset.

To ensure adherence to the aforementioned constraints, we adopted a specific node selection order for constructing each tetrahedron within the unit-cell configuration. This order follows the sequence  $(v_i, f_j, e_k, e_l)$ , where  $i$  ranges from 0 to 3,  $j$  ranges from 0 to 3, and both  $k$  and  $l$  range from 0 to 5. In cases where  $k$  and  $l$  are the same, this indicates that the tetrahedron comprises only two edges. It is important to note that solely utilizing this ordering is insufficient for meeting all constraints; we also enforced these constraints during the coding process. The range of possibilities for various configurations was examined based on the base material Phrozen Onyx Impact Plus, with a Young's modulus of 1.175 GPa, Poisson's ratio of 0.35, and a mass density of 1.15 g/cm<sup>3</sup>, as well as a truss diameter of 0.05. Supplementary Fig 3 illustrates this spectrum, encompassing a total of 528 unique configurations that were generated through the application of the aforementioned constraints.



Supplementary Fig 3: Space of Bulk mechanical properties established from the property search using the 48 tetrahedrons reflection method.

After narrowing down the configurations based on the applied constraints, the subsequent step involves selecting a single unit-cell from those configurations. This selection process should be based on the mechanical properties of the bulk material. The underlying concept behind our approach to selecting a single configuration is to identify a structure that exhibits auxetic behavior among the various topology configurations depicted in Supplementary Figure 3. By modifying the diameter and the offsets of the chosen unit-cell, we can also obtain structures with non-auxetic behavior. Our chosen unit-cell, which serves as the foundation for our parametrization method, is displayed in Fig1. This unit-cell has a Young's Modulus of 1.234 MPa and a Bulk Poisson's ratio of -0.315. It comprises only two edges in each tetrahedron, connecting the  $v_0$ ,  $f_3$ , and  $e_2$  nodes, with a truss diameter of 0.05. The next phase in generating our cubic structures entails sweeping the offsets of the selected unit-cell's nodes and the thickness of its edges across their ranges. We consider these modifications as the initial set of parameters in our parametrization method. Within the tetrahedron, one of the chosen nodes used in constructing the unit-cell, node  $v_0$ , is fixed. Nevertheless, the node  $e_2$  can be positioned at any

location along edge 2, which connects vertices  $v_2$  and  $v_3$ . The offset for this node is determined by a single parameter,  $w_2$ , as presented in Eq S1.

$$e_2 = w_2 v_2 + (1 - w_2) v_3 \quad (S1)$$

The placement of the third node, denoted as  $f_3$ , is flexible on face 3, which is defined as a plane surface constructed by the vertices  $v_0$ ,  $v_2$ , and  $v_3$ . The computation of the coordinates of  $f_3$  is established through barycentric coordinates, as presented in Eq S2

$$f_3 = w_{31} v_0 + w_{32} v_2 + w_{33} v_3 \quad (S2)$$

The final element among the primary set of parameters is the truss radius  $r$ , which varies between 0.02 and 0.05 in our given dataset. In brief, our initial parameterization approach involves five parameters, namely  $w_2$ ,  $w_{31}$ ,  $w_{32}$ , and  $w_{33}$ , with values ranging between 0 and 1, along with the truss radius  $r$ , varying between 0.02 and 0.05. The outcomes of this initial set of parameters yield approximately 4900 unit-cells with a considerable range of bulk mechanical behavior, as illustrated in Fig 2. Nevertheless, this dataset exhibits a limited set of unit-cells, all of which are cubic, thereby not rendering it diverse enough to train a general model.

### Cubic Structure Rotation

Prior to exploring the application of rotations to unit-cells, it is essential to distinguish between the mechanical behavior of the base material and the cellular structures. The orientation of a cubic base material does not impact its stiffness tensor or mechanical properties, as its properties remain isotropic in all directions. However, the stiffness tensor of cellular materials is typically anisotropic, which implies that the mechanical properties are orientation-dependent [2]. This is especially relevant in our study since the numerical homogenization technique used to determine the stiffness tensor was based on six distinct loading scenarios, as previously noted. Thus, if we rotate the cellular material configuration, the stiffness tensor must be adjusted to account for this rotation. As a result, this rotation can potentially transform the cubic cellular structures into highly anisotropic structures exhibiting triclinic behavior. The procedure used to apply rotations is delineated in references [2, 3]. This process can be streamlined by rotating the Voigt notation  $C$  and calculating the Voigt notation of the rotated part, as demonstrated in Eq S3.

$$C_{Rot} = K_R C K_R^T \quad (S3)$$

$$\text{where: } K_R = \begin{bmatrix} K_{R1} & 2K_{R2} \\ K_{R3} & K_{R4} \end{bmatrix}$$

$$K_{R1} = \begin{bmatrix} R_{11}^2 & R_{12}^2 & R_{13}^2 \\ R_{21}^2 & R_{22}^2 & R_{23}^2 \\ R_{31}^2 & R_{32}^2 & R_{33}^2 \end{bmatrix}, K_{R2} = \begin{bmatrix} R_{12}R_{13} & R_{13}R_{11} & R_{11}R_{12} \\ R_{22}R_{23} & R_{23}R_{21} & R_{21}R_{22} \\ R_{32}R_{33} & R_{33}R_{31} & R_{31}R_{32} \end{bmatrix}, K_{R3} = \begin{bmatrix} R_{21}R_{31} & R_{22}R_{32} & R_{23}R_{33} \\ R_{31}R_{11} & R_{32}R_{12} & R_{33}R_{13} \\ R_{11}R_{21} & R_{12}R_{22} & R_{13}R_{23} \end{bmatrix}$$

$$K_{R4} = \begin{bmatrix} R_{22}R_{33} + R_{23}R_{32} & R_{21}R_{33} + R_{23}R_{31} & R_{22}R_{31} + R_{21}R_{32} \\ R_{12}R_{33} + R_{13}R_{32} & R_{13}R_{31} + R_{11}R_{33} & R_{11}R_{32} + R_{12}R_{31} \\ R_{12}R_{23} + R_{13}R_{22} & R_{13}R_{21} + R_{11}R_{23} & R_{11}R_{22} + R_{12}R_{21} \end{bmatrix}$$

The  $R_{ij}$  terms in the rotational matrix can be computed by specifying the rotational angle  $\theta_{\text{rot}}$  and the axis of rotation  $[e_1, e_2, e_3]$ . To generate various configurations of unit-cells, we rotated each of the 4900 unit-cells using an angle  $\theta_{\text{rot}}$ , ranging from  $-\pi$  to  $\pi$ , around the axis of rotation, formed by the combinations of the unit vectors  $e_1$  and  $e_2$ , which range between 0 and 1. The unit vector  $e_3$  for the last axis of rotation was computed using Eq S4. Employing this rotation method, we generated over 3,000,000 unit-cell configurations, many of which exhibit similar behavior. This arises from the base constituent unit-cell's plane of symmetry, where all rotations  $R$  made along the same coordinate axis with an angle of  $k\theta_{\text{rot}}$ , where  $k$  can be -1 or 1, lead to identical configurations and stiffness response.

$$e_3 = \sqrt{1 - e_1^2 - e_2^2} \quad (\text{S4})$$

Using a single angle and axis of rotation can lead to challenges in maintaining continuity in the representation of rotational parameters, as it repeats every  $2\pi$ . This discontinuity renders it difficult to develop data-driven models that directly predict rotational parameters. To address this issue, a feasible solution is to transform the 3D representation  $[\theta_{\text{rot}}, e_1, e_2]$  to a 6D representation using the method proposed by Zhou in [4], employing Eq S5. This conversion enables the representation of each rotation using six continuous parameters, facilitating the development of a data-driven model that predicts rotations. Additionally, it is noteworthy that this method can convert the 6D representation back to a 3D representation if required.

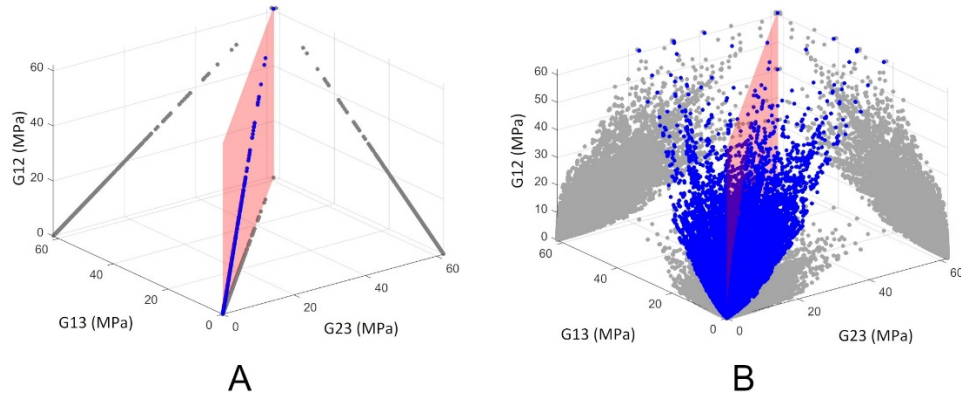
$$R = [b_1 \ b_2 \ b_3] \quad \text{with} \quad b_i = \begin{bmatrix} N(a_1) & \text{if } i = 1 \\ N(a_2 - (b_1 \cdot a_2)b_1) & \text{if } i = 2 \\ b_1 X b_2 & \text{if } i = 3 \end{bmatrix}^T \quad (\text{S5})$$

where  $N(\cdot)$  is a normalization function, and both  $a_1, a_2 \in \mathbb{R}^3$  correspond to the mentioned 6D representation [4]

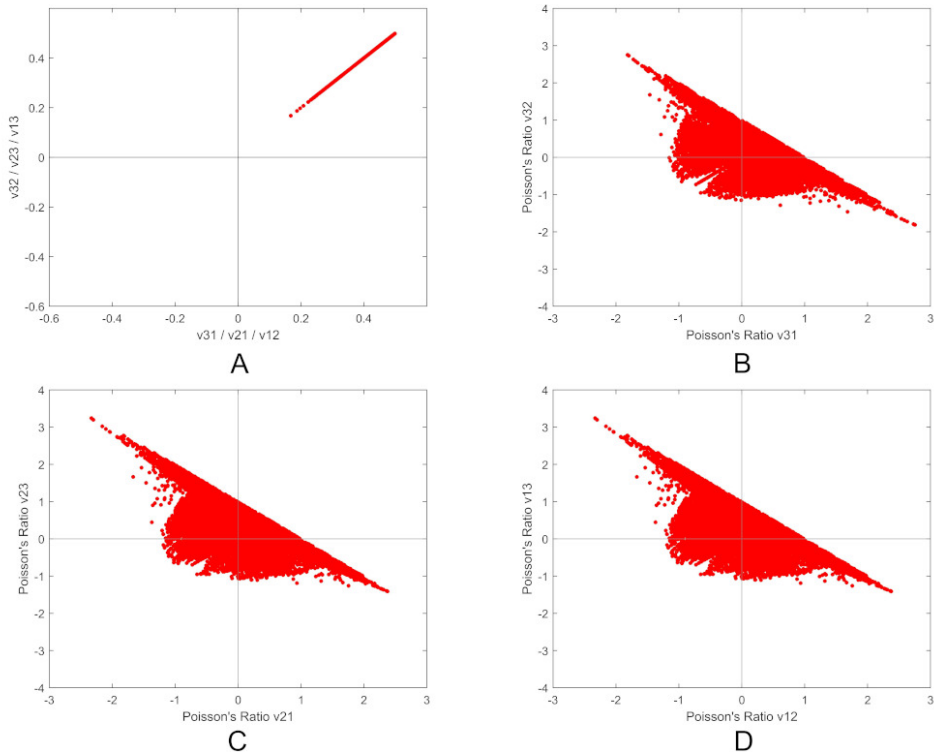
### Dataset Space of Properties

Supplementary Fig 4 and Supplementary Fig 5 illustrate the variations in the elastic property range of our dataset pre and post the application of rotation. Our efforts have culminated in the establishment of a training dataset featuring multiple elastic behaviors, which will be utilized for the training of our inverse design algorithm. The dataset has been parametrized through 11 distinct parameters, encompassing truss thickness ( $r$ ), offset along the second edge of the tetrahedron ( $w_2$ ), and the node's location on the tetrahedron's third surface ( $w_{31}, w_{32}, w_{33}$ ). Additionally, the dataset has been augmented with 6D rotational parameters ( $RR_1, RR_2, RR_3$ ,

$\text{RR}_4$ ,  $\text{RR}_5$ , and  $\text{RR}_6$ ).



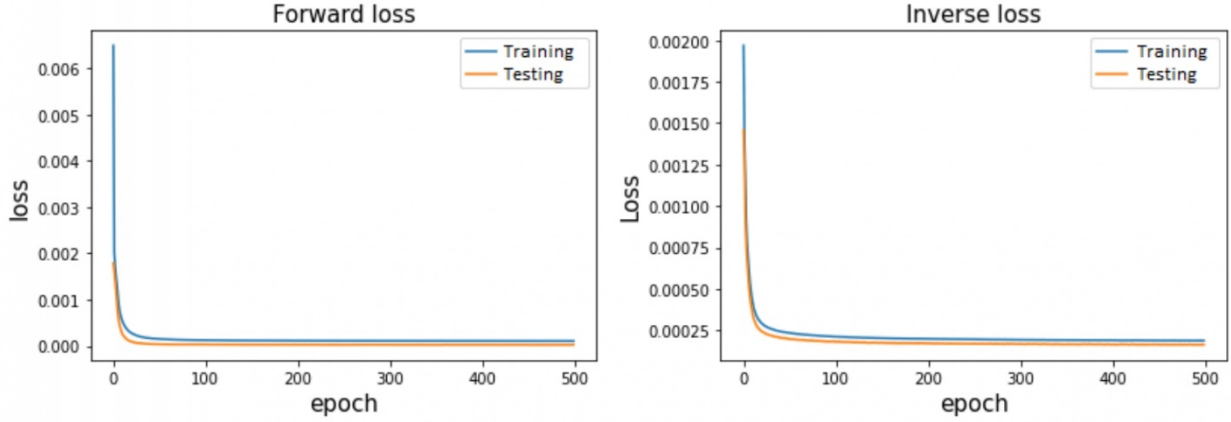
Supplementary Fig 4: Effective Shear Modulus space along the unit-cell axes: A- Cubic configurations without



Supplementary Fig 5: Effective Poisson's ratio space along the unit-cell axes: A- Poisson's ratio along the unit-cell axes for Cubic configurations without rotations, B: Poisson's ratio along axes 1 and 2 when applying force along axis 3 for Cubic configurations after the rotations, C: Poisson's ratio along axes 1 and 3 when applying force along axis 2 for Cubic configurations after the rotations, and D: C: Poisson's ratio along axes 2 and 3 when applying force along axis 1 for Cubic configurations after the rotations.

## Performance Results.

Supplementary Fig 6 offers a comprehensive overview of the training history of our model, showcasing the dynamic changes in both training and testing loss for both inverse and forward models over the course of their training.

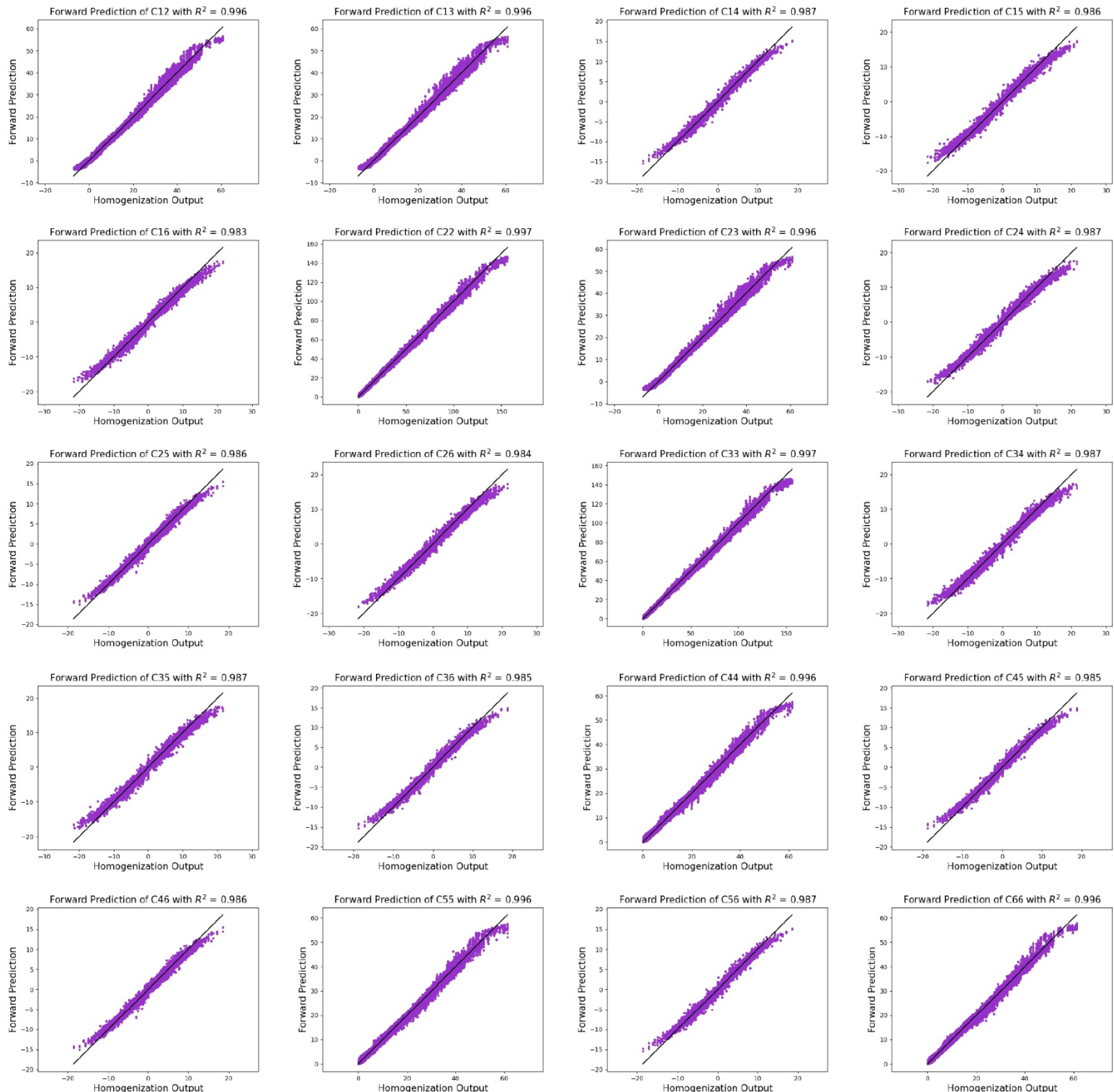


Supplementary Fig 6: Training and testing loss plots of the PGNN: A. Forward loss plot, and B. Inverse.

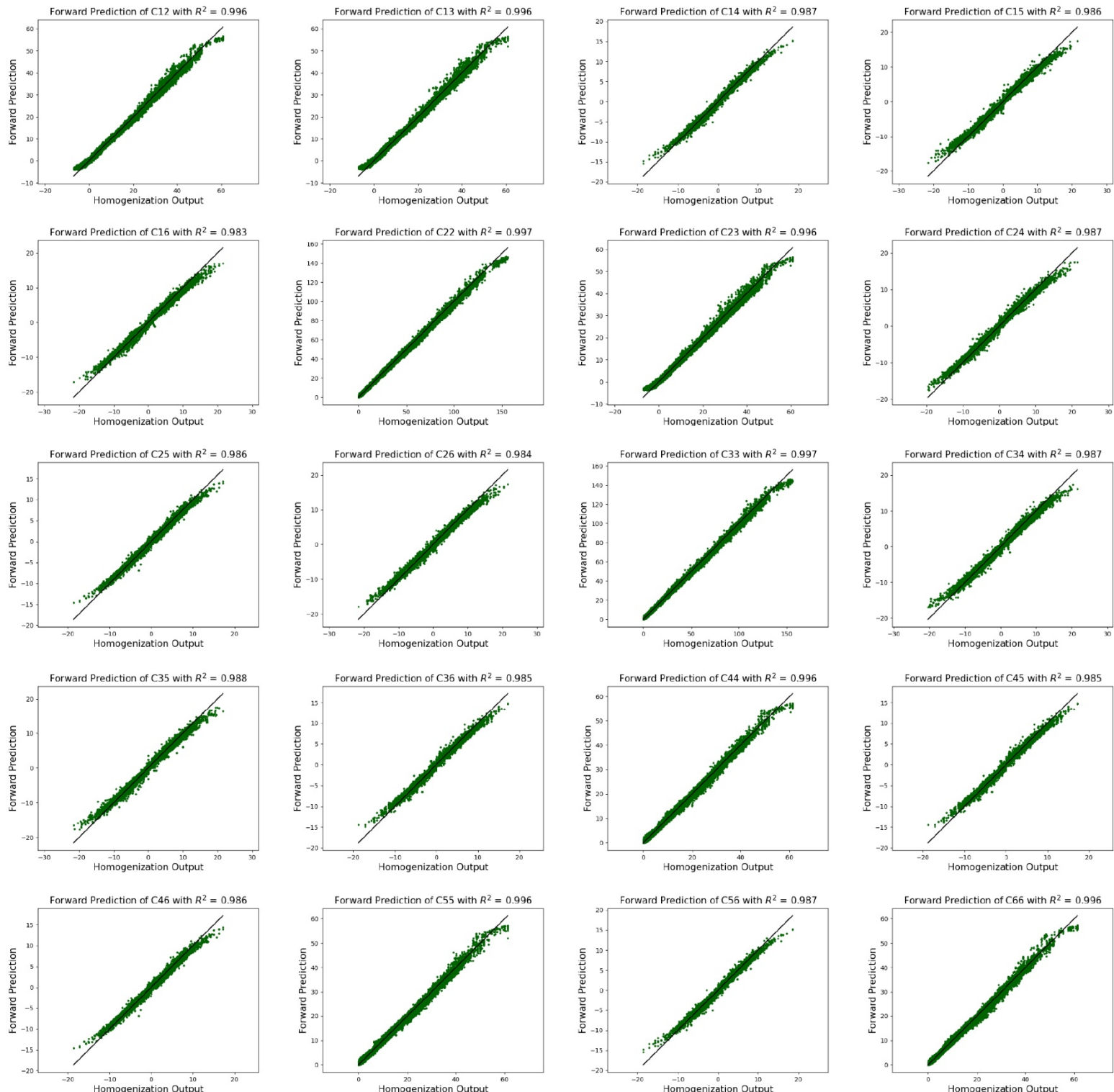
In the main context of this paper, we displayed the accuracy of the  $C_{11}$  reconstruction in Fig. 5. Supplementary Fig 7 through Supplementary Fig 10 provide a comprehensive overview of the entire reconstruction accuracy, excluding  $C_{11}$ , encompassing  $R^2$  values for both forward and inverse models and utilizing both training and testing data. Furthermore, Supplementary Table 1 provides a tabulated listing of all  $R^2$  values.

Supplementary Table 1: Coefficient of determination  $R^2$  of all stiffness components for both the forward and the inverse model, the  $R^2$  is measured for both training and testing sets.

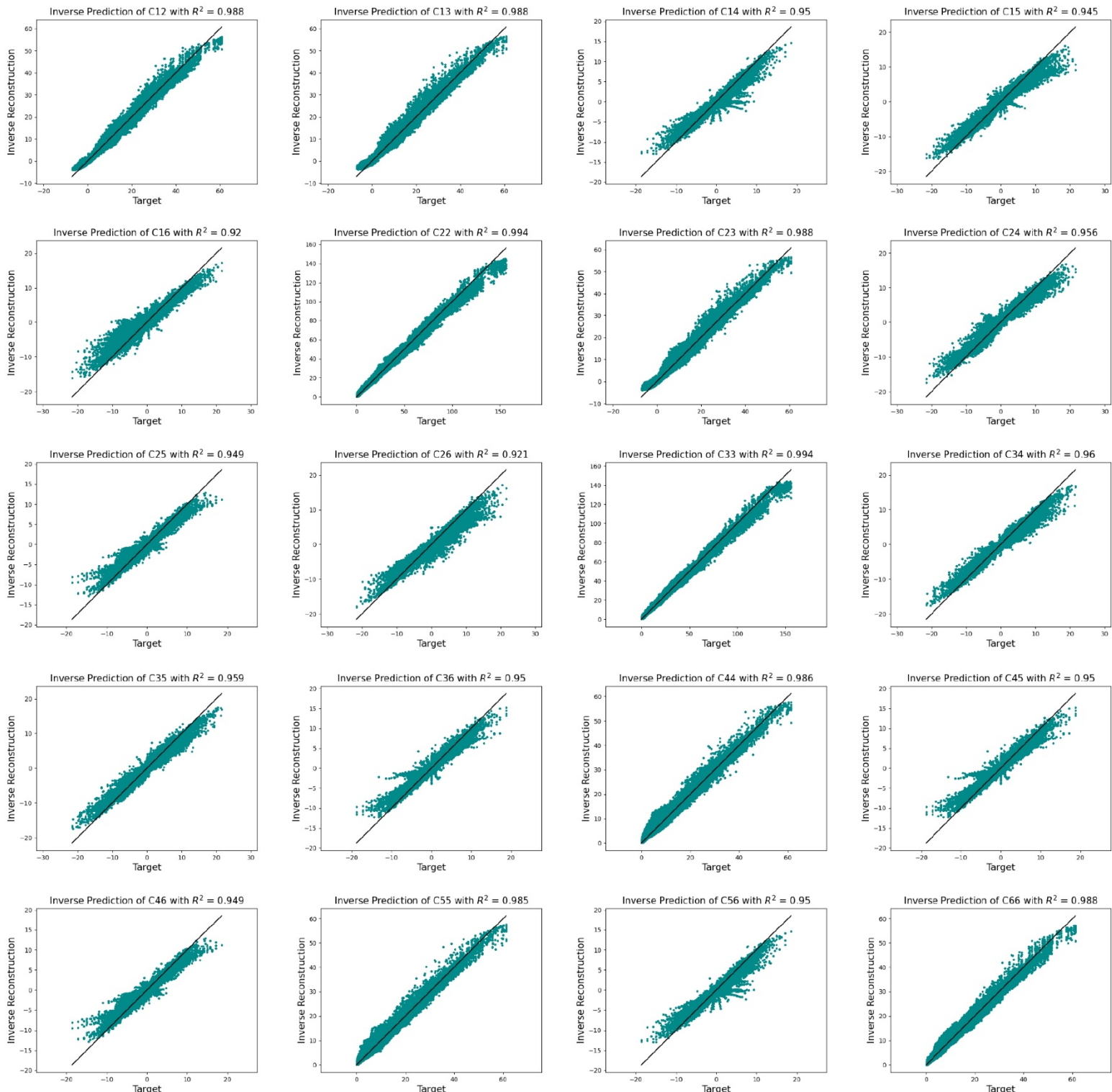
	Forward (Training)	Forward (Testing)	Inverse (Training)	Inverse (Testing)
$C_{11}$	0.998	0.998	0.994	0.994
$C_{12}$	0.996	0.996	0.988	0.988
$C_{13}$	0.996	0.996	0.988	0.988
$C_{14}$	0.987	0.987	0.95	0.951
$C_{15}$	0.986	0.986	0.945	0.945
$C_{16}$	0.983	0.983	0.92	0.92
$C_{22}$	0.997	0.997	0.994	0.994
$C_{23}$	0.996	0.996	0.988	0.988
$C_{24}$	0.987	0.987	0.956	0.956
$C_{25}$	0.986	0.986	0.949	0.948
$C_{26}$	0.984	0.984	0.921	0.921
$C_{33}$	0.997	0.997	0.994	0.994
$C_{34}$	0.987	0.987	0.96	0.961
$C_{35}$	0.987	0.988	0.959	0.959
$C_{36}$	0.985	0.985	0.95	0.951
$C_{44}$	0.996	0.996	0.986	0.986
$C_{45}$	0.985	0.985	0.95	0.951
$C_{46}$	0.986	0.986	0.949	0.948
$C_{55}$	0.996	0.996	0.985	0.984
$C_{56}$	0.987	0.987	0.95	0.951
$C_{66}$	0.996	0.996	0.988	0.988



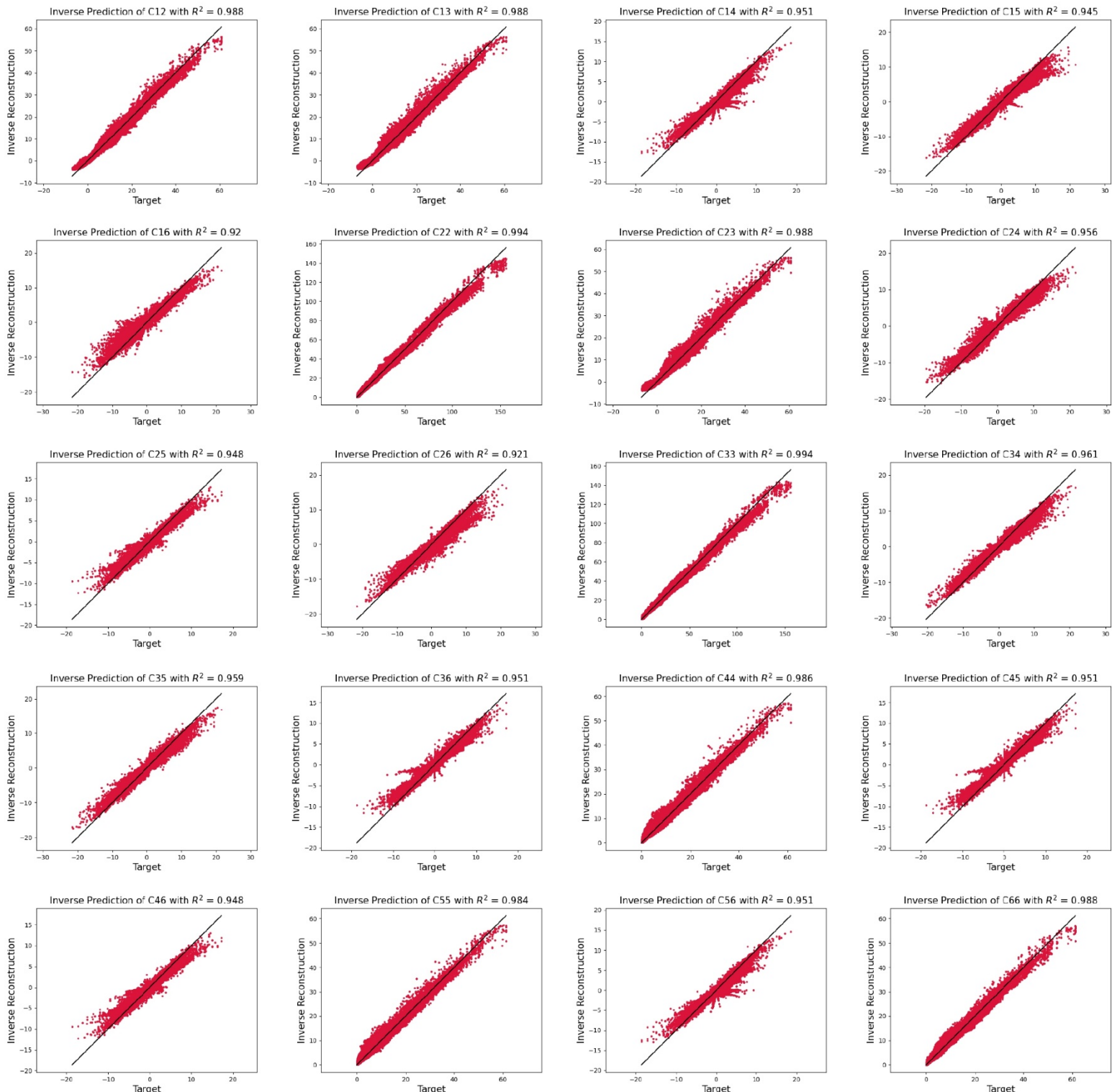
Supplementary Fig 7: Comparing the stiffness components from numerical homogenization with the forward model's predictions for the training data.



Supplementary Fig 8: Comparing the stiffness components from numerical homogenization with the forward model's predictions for the testing data.



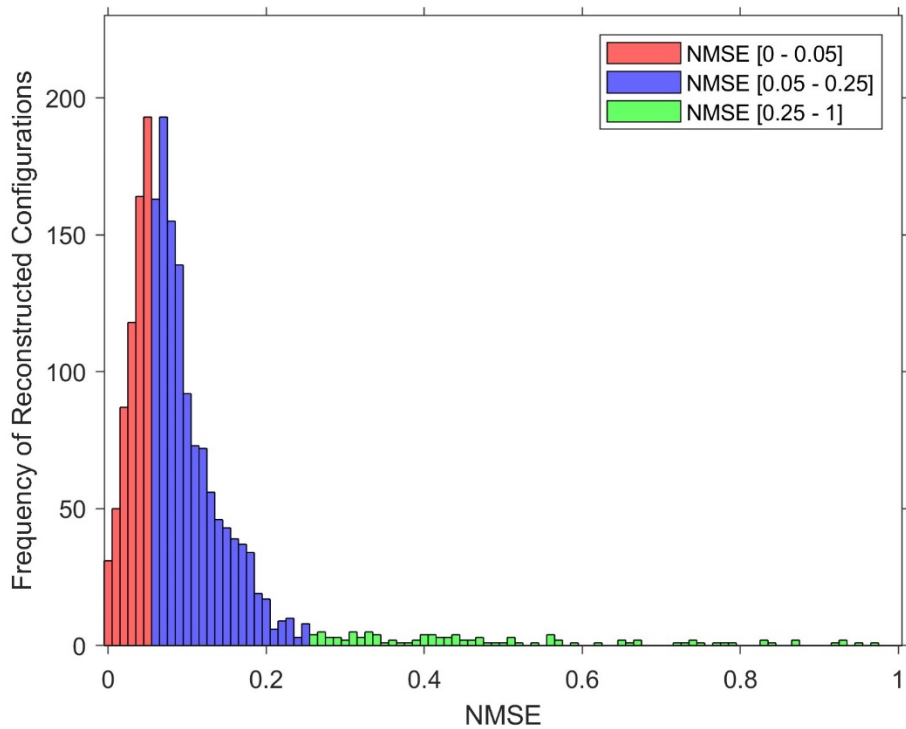
Supplementary Fig 9: Comparing the stiffness components of the target stiffness with the reconstructed stiffness from the inverse model for the training data.



Supplementary Fig 10: Comparing the stiffness components of the target stiffness with the reconstructed stiffness from the inverse model for the testing data.

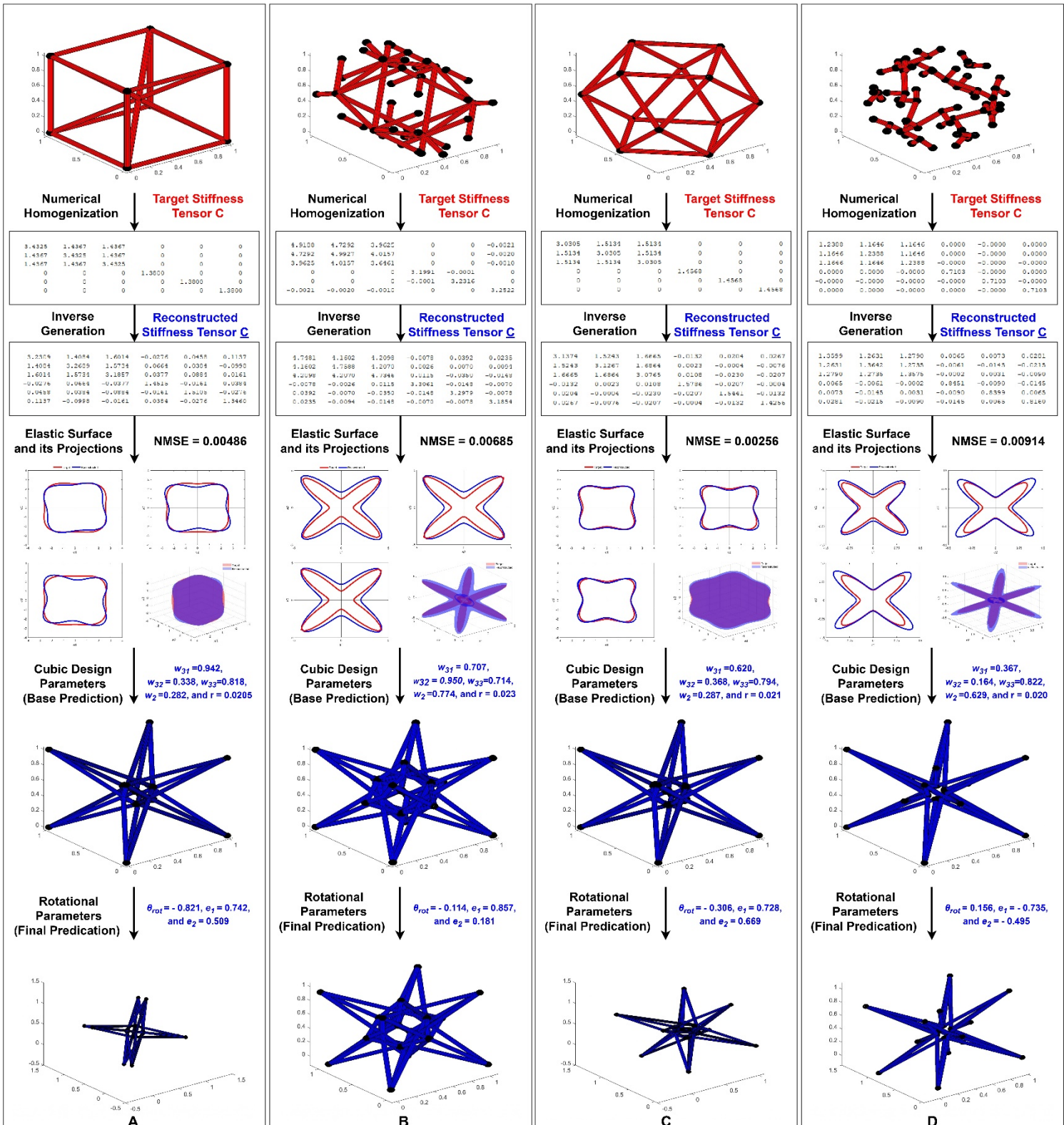
## Network Performance with Lumpe and Stankovic Dataset

In 2021, a dataset was collected that contains a diverse range of topologies, encompassing over 17,000 unique configurations, which exhibit various material behaviors ranging from cubic to triclinic structures [5]. Despite this significant progress, the collected dataset lacks a method for parameterizing this extensive range of configurations. The dataset provides information on the configuration details and normalized homogenized stiffness components, albeit computed at lower densities than our training data range. To address this issue, we have employed the homogenization method mentioned earlier to calculate the homogenized stiffness tensor for a subset of 2000 randomly selected topologies out of the 17,000. The Phrozen Impact Plus material is used as a base material, and a radius of 0.025 is utilized for all the chosen configurations. We subsequently have computed the Normalized Mean Squared Error (NMSE) for reconstructed structures predicted using the inverse framework and have compared them with configurations from the Lumpe and Stankovic dataset. The frequency of each NMSE range is presented in Supplementary Fig 11. The distribution indicates that the model's performance in reconstructing structures with stiffness components similar to the Lumpe and Stankovic dataset is currently inadequate to generalize the method to any configuration, as the reconstruction accuracy is 32% only. Additionally, to exemplify the full inverse design process, four reconstructed configurations with NMSEs lower than 0.05 were randomly selected, and their inverse design process is demonstrated in Supplementary Fig 12.



Supplementary Fig 11: Histogram of the NMSEs of the inversely reconstructed unit-cells based on the stiffness tensor of Lumpe and Stankovic crystallographic trusses dataset.





Supplementary Fig 12: Inverse reconstruction of unit-cells using the stiffness tensor of configurations from the Lump and Stankovic dataset: A. cub\_Z13.3\_E543, B. tet\_Z12.0\_E722, C. cub\_Z08.0\_E877, and D. cub\_Z03.0\_E3050.

- [1] J. Panetta, Q. Zhou, L. Malomo, N. Pietroni, P. Cignoni, D. Zorin, Elastic textures for additive fabrication, *ACM Transactions on Graphics (TOG)* 34 (4) (2015) 1–12
- [2] W. L. Bond, The mathematics of the physical properties of crystals, *The Bell System Technical Journal* 22 (1) (1943) 1–72.
- [3] J.-H. Bastek, S. Kumar, B. Telgen, R. N. Glaesener, D. M. Kochmann, Inverting the structure–property map of truss metamaterials by deep learning, *Proceedings of the National Academy of Sciences* 119 (1) (2022)
- [4] Y. Zhou, C. Barnes, J. Lu, J. Yang, H. Li, On the continuity of rotation representations in neural networks, in: *Proceedings of the IEEE/CVF Conference on Computer Vision and Pattern Recognition*, 2019, pp.
- [5] T. S. Lumpe, T. Stankovic, Exploring the property space of periodic cellular structures based on crystal networks, *Proceedings of the National Academy of Sciences* 118 (7) (2021) e2003504118.